JOURNAL OF PROPULSION AND POWER
Vol. 16, No. 5, September–October 2000

Applied-Field Magnetoplasmadynamic Thrusters, Part 1: Numerical Simulations Using the MACH2 Code

Pavlos G. Mikellides* and Peter J. Turchi†
Ohio State University, Columbus, Ohio 43235
and
Norman F. Roderick‡
University of New Mexico, Albuquerque, New Mexico 87131

Numerical modeling of the NASA Lewis Research Center 100-kW, steady-state, applied-field magnetoplasmadynamic thruster is performed using the magnetohydrodynamics code MACH2 for a range of applied magnetic field strengths and discharge currents. Overall performance trends, obtained experimentally with argon propellant, are captured by the simulations. Magnitudes of plasma voltage vs applied field strength also agree well. Interrogation of the calculated flowfield offers a new visualization of applied-field magnetoplasmadynamic thruster operation, comprising the following elements: 1) the back electromotive force is the dominant contributor to the plasma voltage for the geometry examined; 2) viscous forces oppose applied azimuthal electromagnetic forces and limit the maximum rotational speed to a constant independent of applied field or current value; 3) viscous heating and conversion of thermal energy to axial directed kinetic energy is the main acceleration mechanism; and 4) the low-density, low-conductivity argon plasma for the regime examined does not interact with the applied field in the manner of a magnetic nozzle.

Nomenclature

A = atomic weight, amu
B = magnetic induction, T
e = elementary charge, C
G = shear modulus, kg/m-s^3
g = metric tensor
I = current, A
j = current density, A/m^2
K = thermal conductivity, J/m-s-eV
n = number density, /m^3
P = pressure, J/m^3
Q = numerical viscosity term, J/m^3
$T_{e,I}$ = electron, ion temperature, eV
t = time, s
u = flow velocity, m/s
V = plasma voltage, V
w = azimuthal speed, m/s
δ = Kronecker delta
ε = specific internal energy, J/kg
ζ = number of free electrons/ion
η = electrical resistivity/μ_o, m^2/s
μ = viscosity coefficient, kg/m-s
μ_o = permeability of free space, H/m
ρ = mass density, kg/m^3
σ = stress tensor, J/m^3

Subscripts

e = electron
I = ion
o = neutral
r, θ, z = physical dimensions: radial, azimuthal, axial

Received 11 August 1998; revision received 10 August 1999; accepted for publication 7 September 1999.

*Research Scientist, Aero/Astro Laboratory, 2300 West Case Road. Member AIAA.
†Professor, Department of Aerospace Engineering, Applied Mech. and Aviation, 328 Bolz Hall, 2036 Neil Avenue; currently Senior Research Scientist, U.S. Air Force Phillips Laboratory. Senior Member AIAA.
‡Professor, Department of Chemical and Nuclear Engineering, Farris Engineering Building; currently Senior Research Scientist, U.S. Air Force Phillips Laboratory. Senior Member AIAA.

Introduction

APPLIED-FIELD magnetoplasmadynamic (MPD) thrusters offer specific impulse values that are unattainable by conventional chemical or nuclear propulsion. The simple design and robustness of MPD thrusters are attractive features compared to other electric propulsion devices. The lower current requirement and generally higher exhibited efficiency of applied-field devices also provide an advantage over self-field thrusters for lower power missions. To date however, applied-field MPD thrusters have not consistently demonstrated adequate efficiencies (>30%). This may be caused by insufficient comprehension of acceleration and power loss mechanisms, the latter shown to be dominated by anode power deposition.[1] Research over the last 30 years has mainly been empirical and thus is only able to address the geometries and operating conditions of a limited number of thrusters. Theoretical attempts have not produced models that capture the trends and magnitudes of the experimental data, without resorting to arbitrary assumptions about velocity limits or conversion of rotational energy.

The concept of the applied-field MPD acceleration is based on conversion of rotational (i.e., azimuthal) energy via expansion in a magnetic nozzle. This rotational energy is provided by the electromagnetic force caused by the interaction of the applied in-plane magnetic field and the discharge current as shown in Fig. 1. Induced azimuthal Hall currents interact with the applied magnetic field to produce a radially confining electromagnetic force, $j_\theta B_z$. This confinement in the exhaust region presents the opportunity of azimuthal kinetic energy conversion into axially directed thrust energy. All previous efforts have concentrated in either modeling such a process or providing scaling laws based on the assumption that this type of conversion is the main thrust contributor.

One of the earlier theoretical approaches was that of Krulle[2] who used a simple set of flow equations with an assumed applied-field distribution to study acceleration mechanisms at low current densities and mass-flow rates. The model assumes that the plasma is fully ionized and the self-induced fields are negligible when compared to the applied field. He determined that a considerable part of the total

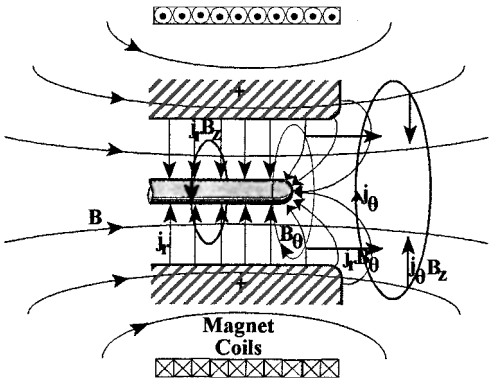

Fig. 1 Applied-field MPD thruster schematic with applied and induced fields and currents and dominating electromagnetic forces shown.

thrust was caused by pressure forces balancing the radial confinement by the $j_\theta B_z$ body force. Substantial azimuthal Hall currents were also calculated well downstream of the thruster's exit. The magnitude of these currents and their persistence downstream of the exhaust plane increased with increasing applied-field strength.

In their treatment of applied-field acceleration mechanisms, Tanaka and Kimura[3] used a two-dimensional set of electromagnetic equations with a quasi-one-dimensional set of fluid equations. This model examined operation with argon propellant at 0.1 g/s, discharge currents of 1000–2000 A and applied field strengths of 0.1–0.2 T at the cathode tip. It showed that substantial Hall currents and plasma rotation were produced from the interaction of the applied field with the discharge current. This plasma rotation was converted to axial momentum via expansion through a magnetic nozzle.

In an experimental study with a 10–35 kW steady-state applied-field MPD thruster using lithium, Fradkin[4] found a linear variation of thrust with the product of discharge current and applied magnetic field strength IB. He also measured large azimuthal Hall currents downstream of the thruster and observed two operating modes for the arc voltage: a high-voltage mode ($I < 400$ A, $\dot{m} < 30$ mg/s), during which the voltage varied parabolically with applied field strength, and a low-voltage mode, in which the same relation was linear. These were explained via a rotating plasma model that assumed the plasma rotates as a homopolar motor. The rotational energy was assumed to be converted completely to axial kinetic energy. This produced simple analytic expressions that scaled thrust as IB and voltage as IB^2 and B for the high- and low-voltage modes, respectively. The latter linear behavior with B was based on the assumption of limiting the rotational speed to Alfvén critical velocity.

The most recent and extensive experimental study of applied-field MPD thrusters was that of Myers[5] with a 100-kW-level steady-state thruster. A wide range of geometries, for argon and hydrogen propellants, was examined for applied field strengths of 0.03–0.2 T at the cathode tip, discharge currents of 750–2000 A, and mass-flow rates of 25–140 mg/s. The observation was made that both thrust and voltage seemed to increase linearly with increasing applied magnetic field strength and discharge current. This was independent of geometry, mass-flow rate, and propellant type. Thrust and discharge voltage increased parabolically with increasing anode radius, but decreased with increasing cathode radius. Thrust magnitudes improved with increasing electrode length, but efficiency decreased. The voltage was independent of cathode length, but increased with decreasing anode length. A significant portion of the power was deposited in the anode for all operating conditions. Thrust efficiencies did not exceed 30%.

Sasoh and Arakawa[6] developed a thrust equation for an applied-field MPD thruster based on energy conservation considerations. They assumed that the work done by the electromagnetic forces is all converted into axial-directed kinetic energy. The acceleration mechanisms considered were Hall, rotational, and self-magnetic accelerations. This formula showed that for moderate applied magnetic field strengths (0.07–0.19 T) the Hall and swirl accelerations are the main thrust contributors for the low discharge currents ($I < 400$ A) and mass-flow rates ($\dot{m} < 30$ mg/s). Comparisons with experiments were limited and constrained by gross assumptions. For higher discharge currents and mass-flow rates the thrust formula underestimates the experimental thrust, suggesting an increasingly important electrothermal component.

The highly interactive physical processes present in the applied-field MPD thruster require a complete theory rather than examination of isolated phenomena or gross assumptions. Solution of the set of equations that include all of the possible relevant physics is necessary. This is one of the objectives of the present paper in which numerical techniques are employed to simulate thruster behavior. Once accomplished, interrogation of the simulated flowfield can define the dominant acceleration process and provide additional insights. A companion paper uses these insights to derive simple analytic expressions for the thrust and voltage that capture trends and magnitudes exhibited in the experiments.

MACH2 Code

MACH2 is a time-dependent, two-dimensional axisymmetric, single-fluid, multitemperature, nonideal radiation, magnetohydrodynamics (MHD) code that has been used to model a variety of laboratory plasma experiments.[7] In all cases the use of the code has allowed better understanding of the physical phenomena involved and had great success in developing ways to improve experimental performance.

The code computes all three components of velocity and magnetic field as functions of the two spatial coordinates. It provides computation in either planar or cylindrical geometry and can manage almost any geometric configuration without any code modification. This broad geometric class of domains is handled by division of the physical domain into appropriate block-like regions, which in turn are transformed into logical rectangular blocks that make up the computational domain.[8] Initial conditions require the input of mass density, temperature(s), and applied magnetic field for each physical block.

MHD Equations

The single-fluid MHD equations used in MACH2 include the continuity equation, the momentum equation in three-vector form, a set of energy equations, and the magnetic field transport equation (Summation is indicated by repeated indices.):

Continuity:

$$\frac{\partial \rho}{\partial t} = -\left[u^i \nabla_i \rho + \rho \nabla_i u^i\right] \tag{1}$$

Momentum:

$$\rho \frac{\mathrm{D}u^i}{\mathrm{D}t} = \nabla_j \left[(-P + Q)g^{ij} + \sigma^{ji}\frac{1}{\mu_o}\left(B^j B^i - \frac{1}{2}B^2 g^{ji}\right)\right] \tag{2}$$

where the stress tensor was only appropriate to handle material strength. This was revised to model a viscous isotropic fluid that upgraded the code into a Navier–Stokes solver:

Electron specific internal energy:

$$\rho \frac{\mathrm{D}\varepsilon_e}{\mathrm{D}t} = -P_e g^{ji}\nabla_i u^j + \eta_{ij} J^2 g^{ij} + \nabla_i\left(k_e^{ij}\nabla_j T_e\right) - \dot{q}_{\mathrm{rad}} - \rho v_{\mathrm{el}}(\varepsilon_e - \varepsilon_I) \tag{3}$$

where v_{el} is the thermal equilibration frequency. The radiation models available include radiation cooling in optically thin limit and equilibrium radiation diffusion along with a nonequilibrium radiation diffusion theory.

Ion specific internal energy:

$$\rho \frac{\mathrm{D}\varepsilon_I}{\mathrm{D}t} = \left[-(P_I + Q)g^{ji} + \sigma^{ji}\right]\nabla_i u_j + \nabla_i\left(k_I^{ij}\nabla_J T_I\right) + \rho v_{\mathrm{el}}(\varepsilon_e - \varepsilon_I) \tag{4}$$

Magnetic induction:

$$\frac{\partial \boldsymbol{B}}{\partial t} = \bar{\nabla} \times (\boldsymbol{u} \times \boldsymbol{B}) - \bar{\nabla} \times (\eta \bar{\nabla} \times \boldsymbol{B}) - \bar{\nabla} \times \frac{1}{e\mu_o n_e}(\bar{\nabla} \times \boldsymbol{B} \times \boldsymbol{B}) \tag{5}$$

The set of equations is closed with the addition of an equation of state and a caloric equation of state that prescribe the species' pressure and specific internal energy in terms of the species' number densities and temperatures. They can be either analytical or tabular; the analytical equations include the ideal gas model and a model appropriate for solids. The tabular model[9] in the code is the SESAME Equation-of-State Library.[10] Its database includes the standard thermodynamic quantities, along with the fractional ionization state based on local thermodynamic equilibrium and transport coefficients. The tabular look-up aspect of the code is easily adapted to input tabular equation of state models supplied by the user.

Transport Coefficients

The viscosity coefficient model was upgraded to a two-temperature, partially ionized gas that contains s number of different heavy species of approximately equal mass m; it is given by[11]

$$\mu = \frac{1}{2}\alpha m \bar{C} \sum_{i=1}^{s} n_i \lambda_i \tag{6}$$

where $\bar{C}$ is the mean thermal speed, n_i is the number density, λ_i is the mean free path, and α is a numerical factor equal to 0.998. The model assumes that for a degree of ionization between zero and one only atoms and single ions constitute the gas, for a degree of ionization between one and two only single and double ions exist in the plasma, and so on, up to an unlimited degree of ionization.[12] The ion thermal conductivity model was also improved in consistency with the aforementioned model, under the assumption of a constant Prandtl number of $\frac{2}{3}$:

$$K_I = \frac{fk}{(\gamma - 1)m}\mu \tag{7}$$

where f is a factor equal to 2.5 (it never exceeds 2.511 for atoms repelling each other with a force that varies inversely with some power of the distance, and it never exceeds 2.522 for rigid elastic spheres[11]), k is the Boltzmann constant, and γ is the ratio of specific heats. The classical Spitzer–Härm model[13] is implemented for the electron thermal conductivity

$$K_e = \frac{3.103 \times 10^4 [4.1 - 15.5/(4 + \zeta)] T_e^{\frac{5}{2}}}{\zeta^2 \ell n \Lambda} \text{ (J/m-s-eV)} \tag{8}$$

where A is the atomic weight, $\ell n \Lambda$ is the Coulomb logarithm, and ζ is the number of free electrons per ion ($\zeta \geq 1$ when used in these models).

The electrical resistivity models simulate both classical particle-particle interactions and anomalous particle-turbulent fields interactions. The classical component is based on the Spitzer–Härm[13] model for fully ionized gas:

$$\eta_\perp = 1.0328 \times 10^{-4} \left(\zeta \ell n \Lambda \Big/ T_e^{\frac{3}{2}} \right) \tag{9}$$

under the confirmed assumption that Coulomb collisions dominate. The anomalous resistivity model[14,15] used for the present calculations is based on the assumption that the lower-hybrid drift microinstability is the dominant contributor to any particle-wave interactions—appropriate for plasmas confined by magnetic fields—and adds to the preceding classical value

$$\eta_a = \frac{0.7 m_e}{e\sqrt{\varepsilon_o}} \sqrt{\frac{A}{\rho \bar{\zeta}}} (1 - e^{-u_{de}/u_{ia}}) \left(1 + 0.3 \frac{u_{de}}{u_{ia}} \sqrt{\frac{B^2}{B^2 + C\zeta\rho/A}} \right) \tag{10}$$

where u_{de} is the electron drift speed, u_{ia} is the ion acoustic speed, and $C = 6.1544 \times 10^7$ m^3-T^2.

Boundary Conditions

Application of the boundary conditions in MACH2 is carried out by the ghost-cell technique, discussed in more detail later, which eliminates the need for special boundary differencing expressions.

Magnetic field boundary conditions include appropriate expressions for idealized conductor and insulator surfaces and the axis of cylindrical symmetry. For steady-state problems the poloidal magnetic field boundary conditions have to allow evolution in response to azimuthal currents generated and sustained by the plasma in addition to any other applied fields generated by external coils. This new model was integrated into the code via the Biot–Savart law under the assumption that individual cells generated by the computational grid act as circular, current-carrying filaments that contribute to the total poloidal field at the boundaries.[12] Any external field coil windings add their contributions in the same manner. Hydrodynamic boundary conditions can be either free-slip or no-slip, whereas thermal conduction boundary conditions can also be of two types: no heat flux (adiabatic) or conduction to a fixed wall temperature. Modeling of inlets requires input of the inlet temperature(s), density, and velocity, whereas at an outlet the conditions inside the boundary determine the state outside by not allowing any gradients perpendicular to the boundary. The axis of cylindrical symmetry reflects that the conditions just outside the problem boundary are the mirror image of those just inside of it.

Numerical Scheme

The physical model described in the preceding sections is solved numerically by a time-split, time-marching algorithm. Time splitting consists of the sequential application of separate portions of a system of equations, rather than the simultaneous application of the entire set. The thermal and equilibrium radiation diffusion, resistive diffusion, and the Lagrangian hydrodynamics are done with implicit time differencing, whereas radiation cooling, coordinate system motion, convective transport, and the Hall effect are carried out with explicit differencing. MACH2 controls the time step such that the stability of the explicit differencing is maintained.

The finite volume approach is used for the spatial differencing formulas. The adaptive ideal coordinate system is generated by solving a variational problem of the block complex using a weight function selected from a standard family of user-specified parameters. The grid's subsequent motion uses an arbitrary-Lagrangian-Eulerian approach. This allows it to move in either Lagrangian, Eulerian, or arbitrary fashion with respect to the fluid. This method provides a means of avoiding negative aspects that can arise from purely Lagrangian (coordinate distortion) or purely Eulerian (numerical diffusion) calculations, while providing higher resolution in regions of physical interest and solution confirmation.

Application of the boundary conditions and communication between neighboring blocks that make up the computational domain are carried out by the ghost-cell technique. Each side of a block's boundary is extended by one more row of cells, the ghost cells to which the special boundary conditions are applied. Then the full difference equations can be applied to points on the region boundary just as to the interior points because the region containing data is larger than the physical region.

Numerical Modeling

MACH2 was used to simulate a steady-state, applied-field, argon MPD thruster at the NASA Lewis Research Center because of the wide range of experimental data[5] (also, personal communication by R. M. Myers, Svedrup Technology, Inc., Lewis Research Center Group, 1994) available. The baseline configuration, shown in Fig. 2, consists of a 1.27-cm radius cathode and a 5.1-cm radius anode, both of which are 7.6 cm long. The magnet coil that provides the applied field is 15.3 cm long with a 10.15-cm radius and is placed with one end flush with the exit plane. The experimental operating conditions simulated at the inlet were argon propellant at 0.1 g/s under the assumption of uniform mass injection at the backplate. The applied magnetic field strength was varied from 0.034 to 0.102 T, as measured at the cathode tip, and the discharge current

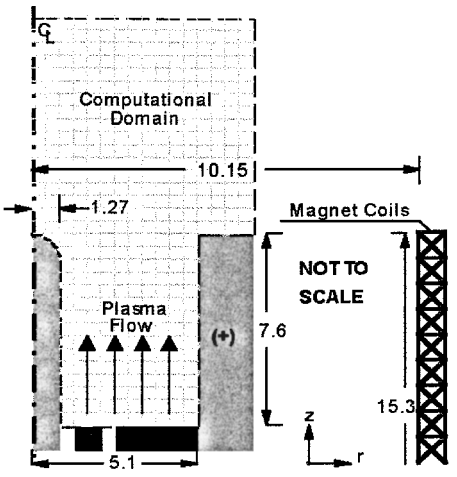

Fig. 2 Geometry of the NASA LeRC applied-field MPD thrusters simulated. The computational domain is encompassed by the dashed lines extending 20 cm downstream of the thruster's exit. Dimensions are in centimeters.

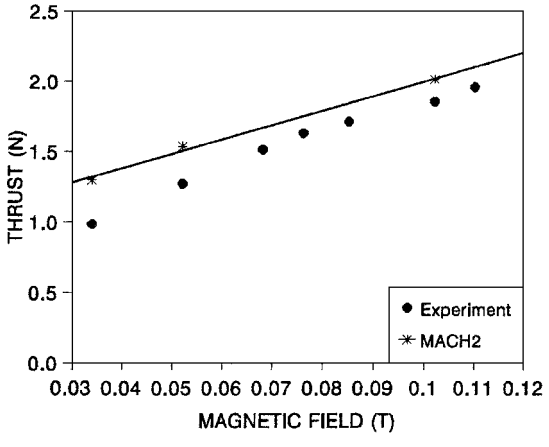

Fig. 3 Thrust vs applied magnetic field strength (at the cathode tip). Argon at 0.1 g/s and discharge current of 1000 A.

from 750 to 1250 A. The fluid formulation was two-temperature, viscous, with real equations of state. No slip was assumed at the walls, and the cathode and anode were fixed at temperatures of 0.2 and 0.1 eV, respectively. The partially ionized gas viscosity and thermal conductivity models, along with the anomalous electrical resistivity model already outlined, were incorporated. The computational grid was Eulerian and extended 30 cm downstream of the backplate with 12×14 cells resolving the discharge chamber. The plume region was more coarsely resolved in the axial direction with outlet boundary conditions, excluding of course the axis of symmetry.

Overall Modeling

The five steady-state cases computed provide thrust and plasma voltage variations with respect to applied magnetic field strength and discharge current. The very-low-density environment typical of these thrusters along with the explicit formulation of the Hall effect resulted in quite a computationally adverse series of simulations. Numerical time steps were limited to the order of a few nanoseconds, but steady state typically was not attained until half a millisecond of operation. This in turn implies that numerical energy losses and errors may be increased, as compared to unsteady problems, because of the increased number of cycling through the full set of equations.

Thrust is computed at the outlet boundaries of the computational region, the results of which are compared with experiments in Figs. 3 and 4. The seemingly linear increase of thrust with applied field and discharge current is apparently captured by the theory, suggesting that the main acceleration mechanisms which provide such behavior are included in MACH2.

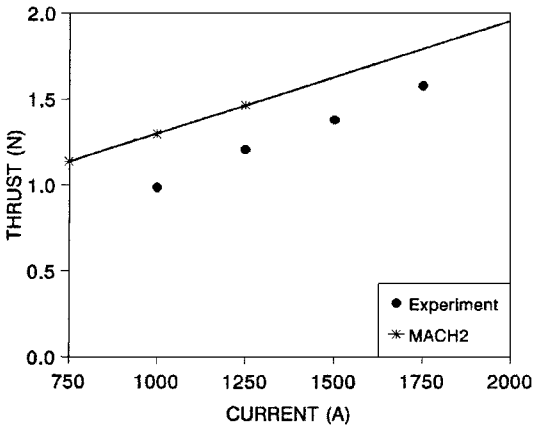

Fig. 4 Thrust vs discharge current. Argon at 0.1 g/s and 0.034 T (at cathode tip).

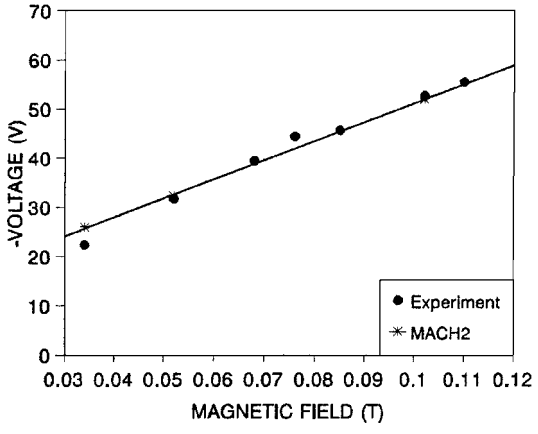

Fig. 5 Plasma voltage vs applied magnetic field strength (at the cathode tip). Argon at 0.1 g/s and discharge current of 1000 A.

Plasma voltage is defined as the discharge voltage excluding fall voltages. Fall voltages occur within sheath regions in the proximity of the electrodes and were experimentally obtained by proper reduction of the calorimetrically measured power lost to these electrodes.[5] MACH2 predictions are compared with experimental data in Fig. 5. The linear voltage dependence on the applied-field strength is accurately predicted, establishing that the manner by which energy is deposited in the plasma is contained in the MACH2 physics.

The discrepancies of the thrust computations with experiment may be qualitatively attributed to erroneous calculations of a very low-density region extending from the cathode tip. Besides the fact that in general such a region is governed by a specialized set of physics, the spinning exhausting plasma demands minimum density in this area possibly rendering it outside the overall MACH2 continuum assumption. Plasma voltage calculations do not share the discrepancies because they do not include the cathode tip region. Unless specialized models are included in MACH2 to transition calculations properly to such regions the discrepancy cannot be quantified. Similarly, total voltage calculations could not be performed because MACH2 does not include the specialized sheath models necessary to resolve regions in the electrode vicinity. However, the comparisons with experiment do provide enough confidence to extract useful insights as to the thruster's overall operation.

Detailed Modeling

With a considerable amount of confidence in the predictive capabilities of the theory, we now proceed to interrogate the basic flowfield properties with the following objectives: identify the main plasma energy deposition source(s), explain the dependence of voltage on controlled external parameters, and identify the main

acceleration mechanism(s). These will be accomplished by examining the distributions of the principal variables in both the discharge chamber and plume for the 0.102 T, 1000 A simulated case.

Figures 6 and 7 depict the two-dimensional distributions of the enclosed current contours, magnetic flux, azimuthal speed, and in-plane velocity vectors. We note a small distension of current downstream of the exit plane, allowing an accurate calculation of the total applied azimuthal electromagnetic force by integration of the body force over the chamber's volume. This results in a total force of 3.486 N, which shows the insignificance of current distribution when compared to a simple calculation of $IB(r_a - r_c)$ of 3.91 N. The rotational force implies expected azimuthal speeds (at 0.1 g/s) in the excess of 30 km/s. The expected magnitudes, however, are contradicted by the calculated ones (Fig. 7), which never exceed 11 km/s. This implies the existence of an opposing force, which the azimuthal momentum equation suggests can only be viscous drag. In addition other acceleration mechanisms (besides conversion of azimuthal kinetic energy to axial energy) are needed to account for the generally higher axial speeds depicted in the vector display (Fig. 7). In-plane velocity vectors also exhibit the sudden turn and loss of axial momentum consistent with flow negotiating a boundary layer. Self-field acceleration is excluded as an explanation for this additional acceleration because its value is only 0.08 N. The aforementioned statement is supported by the electron and ion temperature distributions (Fig. 8), which show that the plasma consists of a hot ion gas and a moderate-temperature electron gas. The elevated ion temperatures suggest a direct mechanism for heating the ions (as opposed to Joule heating and subsequent thermal equilibration with the electrons), namely viscous heating. The magnitudes of the ion temperatures further imply that these viscous effects are quite significant. The

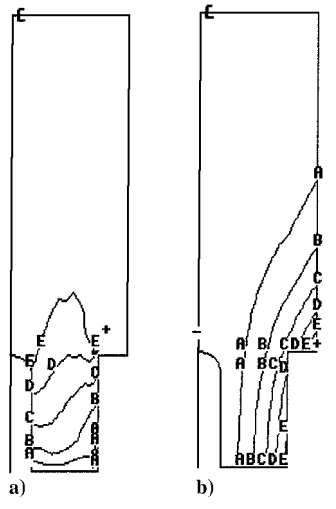

Fig. 6 Two-dimensional distributions for B_c = 0.102 T and I = 1000 A. a) Enclosed current, rB_θ (A)—min(−) = −660, A = −540, B = −410, C = −290, D = −160, E = −40, max(+) = 85. b) Magnetic flux lines (Weber)—min(−) = -6.7×10^{-5}, A = 1.8×10^{-4}, B = 4.2×10^{-4}, C = 6.6×10^{-4}, D = 9.1×10^{-4}, E = 1.1×10^{-3}, max(+) = 1.4×10^{-3}.

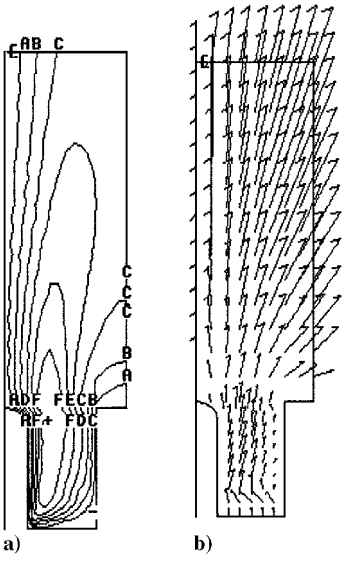

Fig. 7 Two-dimensional distributions for B_c = 0.102 T and I = 1000 A. a) Azimuthal velocity (km/s)—min(−) = −0.42, A = 1.2, B = 2.9, C = 4.5, D = 6.2, E = 7.8, F = 9.5, max(+) = 11. b) In-plane velocity (km/s)—max = 14.49.

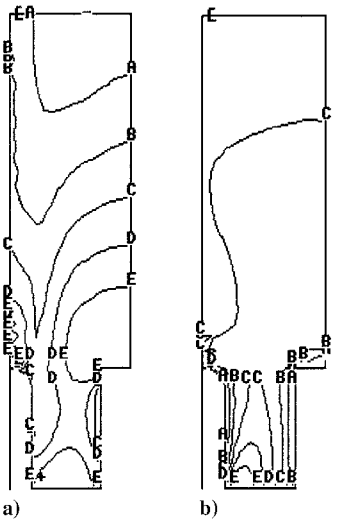

Fig. 8 Two-dimensional distributions for B_c = 0.102 T and I = 1000 A. a) Ion temperature (eV)—min(−) = 0.86, A = 1.2, B = 1.8, C = 2.7, D = 3.9, E = 5.6, max(+) = 8.2. b) Electron temperature (eV)—min(−) = 0.74, A = 1.0, B = 1.3, C = 1.5, D = 1.8, E = 2.1, max(+) = 2.4.

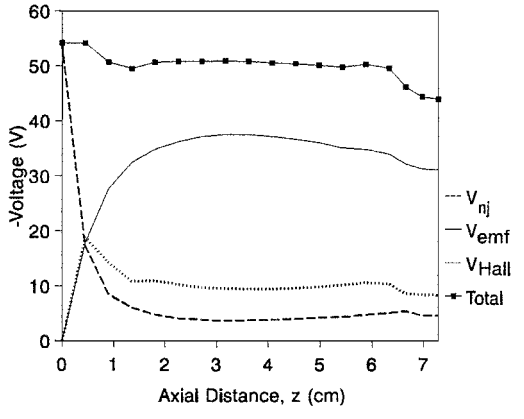

Fig. 9 Plasma voltage contributions for the 0.102 T, 1000 A case.

importance of viscous effects in limiting the attainable rotational speeds and providing the heavy particle heating can be easily seen by a simple calculation of the Reynolds ($Re = \rho U L/\mu$) and Hartmann [$H = BL/\sqrt{(\mu\eta)}$] numbers. The former is of the order of 10, suggesting that viscous forces are quite significant when compared to inertial forces, and the latter is also of the order of 10, exhibiting the importance of viscous forces when compared to electromagnetic forces.

We note from Fig. 9 that the back emf contribution to the plasma voltage is the dominant one despite the speed limitation. This was consistent for all of the cases simulated. The Hall effect and resistive drop account for 14 V of the total voltage, as opposed to 40 V caused by a spinning plasma. A further insight in the behavior of the rotational speed as a function of the applied electromagnetic force is drawn by inspection of Fig. 10. As the azimuthal force is increased, the maximum speed reaches a limiting value rather than increasing linearly with the force for constant mass-flow rate. This is not only consistent with a fully developed flow that shows the dramatic effects of viscosity, but also explains the linear increase of voltage with applied field and constancy with discharge current when combined with the fact that the back emf dominates.

$$\text{Unlimited rotation: } w \sim IB \Rightarrow V \sim wBf(r) \sim IB^2 f(r)$$

$$\text{Limited rotation: } w \sim c \Rightarrow V \sim wBf(r) \sim cBf(r) \quad (11)$$

where $f(r)$ is some function accounting for the profile effects and c is a constant.

This limitation should have profound effects on propellant acceleration as well, especially if conversion of azimuthal kinetic energy to thrust energy is substantial. This conversion can only be accomplished if plasma expansion from the chamber occurs in a manner of a properly designed nozzle. An insight to the degree of such confinement by the electromagnetic force $j_\theta B_z$ is given by calculation

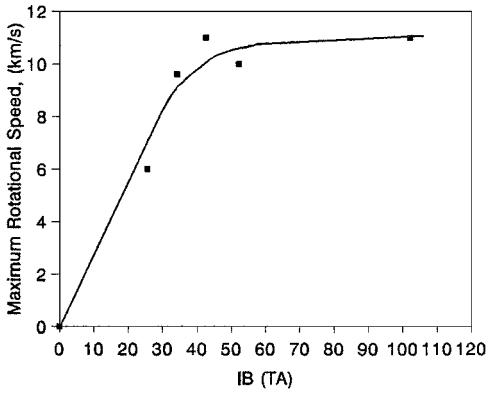

Fig. 10 Maximum rotational speed vs discharge current × applied magnetic field.

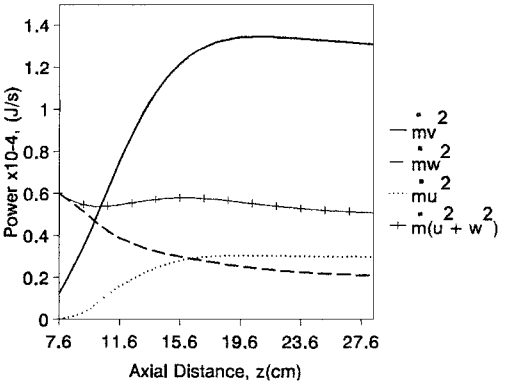

Fig. 12 Power distribution as a function of axial distance for the 0.102 T, 1000 A case.

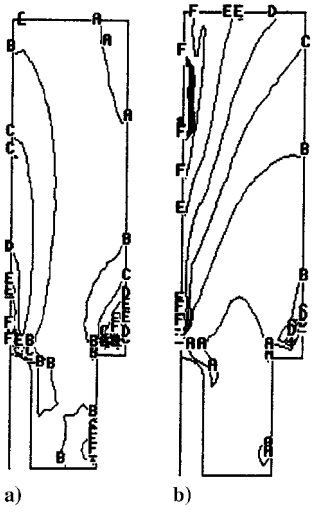

Fig. 11 Two-dimensional distributions for B_c = 0.102 T and I = 1000 A. a) Electron Hall parameter—min(−) = 0, A = 1, B = 2, C = 3, D = 4, E = 5, F = 6, max(+) = 7. b) Anomalous/classical electrical resistivity ratio—min(−) = 0, A = 7, B = 14, C = 21, D = 28, E = 35, F = 42, max(+) = 49.

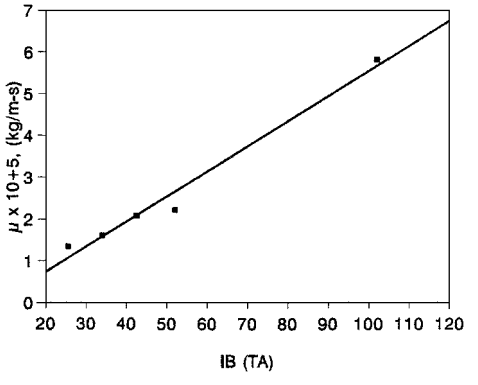

Fig. 13 Viscosity coefficient vs the product of discharge current and applied magnetic field.

of the electron Hall parameter Ω and the actual electrical resistivity of the plasma. Distributions of the Hall parameter and the ratio of anomalous-to-classical resistivity as calculated by MACH2 are depicted in Fig. 11. They show the dramatic effects of anomalous contributions as the Hall parameter for the main plasma expanding core is only 2. The consequences can be readily seen when one compares this value to the magnitudes of $16 < \Omega < 100$ that can be obtained by excluding anomalous resistivity effects. Although the latter may imply the capability of inducing strong azimuthal currents that will create the magnetic nozzle, the former show that this capability is quite diminished, especially when combined with the fact that current distension downstream of the exit is insignificant (Fig. 6). In addition, the magnetic Reynolds number (including anomalous effects) never exceeds the moderate value of 0.3, which implies inadequate interaction of plasma and field. This is supported by plume density distribution data[16] that do not follow magnetic field lines. The same experiments, however, indicate that confinement is implied because of increased radial density gradients with increasing field. This trend can be explained by realizing that the exiting spinning plasma will maintain inertial pressure gradients for some distance downstream of the exit, the magnitudes of which are proportional to the applied magnetic field strength. These radial pressure gradients are confining, but independent of the magnetic field lines. The lack of magnetic confinement is confirmed by a detailed accounting of the azimuthal and radial kinetic energy in the plume region. This is carried out in Fig. 12 and shows that the sum of azimuthal and radial kinetic energies is constant as a function of axial distance downstream of the thruster's exit. Thus, the azimuthal kinetic energy is mainly converted to radial kinetic energy consistent with an unconfined expansion. Based on the same energy accounting, in conjunction with the ion temperature distribution in the plume region (Fig. 8) the main acceleration mechanism is the conversion of thermal energy, provided by viscous heating, to axially directed kinetic energy. Specifically, the averaged ion temperature at the exit ($T \sim 5$ eV) implies that $2\dot{m}CpT \sim 1.34 \times 10^4$ J/s accounting for the maximum value of $\dot{m}v^2$ in Fig. 12.

The significance of viscous effects in these low-density thrusters warrants further investigation. Variation of the mass-flow-averaged viscosity coefficient at the exit of the thruster as the applied azimuthal electromagnetic is increased is depicted in Fig. 13 and provides a nonintuitive, yet extremely important, result. The ratio of IB/μ is constant and defines the limiting characteristic rotational speed, subject only to profile effects. The value of this ratio is 1.667×10^6 m/s for this particular geometry and operating conditions. This can be explained by the following argument: as IB increases, the heavy particles are heated directly by viscous forces. Electron temperatures, however, remain moderately constant—along with density[12]—implying an approximately constant degree of ionization. Under such conditions the viscosity coefficient is an increasing function of ion temperature. It is calculated by the MACH2 model that this function is the same as the one by which ion temperature increases as IB is elevated. It is readily apparent that such an insight would never have been captured if the viscosity coefficient model developed for these simulations did not include two-temperature effects.

Conclusions

Simulations of a steady-state, applied-field, argon MPD thruster[5] at NASA Lewis Research Center using the time-dependent, two-dimensional, axisymmetric, MHD MACH2 provided thrust and plasma voltage values that were compared with the experimental ones. Predicted thrust for a range of applied magnetic field strengths and discharge currents overestimated the experimental data, but captured the ostensible linear increase of thrust with both applied field and current. Plasma voltage predictions, excluding electrode falls, captured both the magnitude and linear increase with increasing magnetic field strength.

For the operating geometry and conditions examined calculations indicate that the radially confining electromagnetic forces are inadequate for magnetic nozzle behavior. The low-density, moderate Hall parameter ($\Omega \sim 2$) plasma was highly resistive ($\eta_a / \eta_{cl} \sim 10$), especially in the exhausting plume region, and thus did not sufficiently interact ($Rm_{max} \sim 0.3$) with the in-plane magnetic field. The electromagnetic azimuthal force applied to the plasma is opposed by viscous forces that limit the maximum attainable rotational speed to magnitudes much smaller than values expected only from inertia. The main acceleration mechanism was found to be conversion of thermal energy, developed largely by viscous heating, as the plasma exhausted from the discharge chamber. The limitation of the maximum rotational speed in conjunction with the dominance of the back electromotive force of the plasma voltage explains the linear dependence of the latter of applied magnetic field strength and the constancy of plasma voltage under varying discharge current. These new insights can be used to develop simple analytic expressions that predict thrust and voltage, which in turn can identify specific avenues for improving performance.

Acknowledgments

The authors acknowledge the support of the NASA Lewis Research Center (LeRC) under Grant NAG843 and the Ohio Supercomputer Center. We especially thank Roger M. Myers for his personal interest and assistance with the NASA LeRC thruster data.

References

[1]Myers, R. M., "Anode Power Deposition in Applied-Field MPD Thrusters," AIAA Paper 92-3463, July 1992.

[2]Krulle, G., "Theoretical Treatment of Current, Mass Flow, and Related Distributions in MPD Plumes," AIAA Paper 72-501, July 1972.

[3]Tanaka, M., and Kimura, I., "Current Distribution and Plasma Acceleration in MPD Arcjets with Applied Magnetic Fields," *Journal of Propulsion and Power*, Vol. 4, No. 5, 1988, pp. 428–436.

[4]Fradkin, D. B., "Analysis of Acceleration Mechanisms and Performance of an Applied Field MPD Arcjet," Ph.D. Dissertation 1088-T, Dept. of Mechanical and Aerospace Engineering, Princeton Univ., Princeton, NJ, March 1973.

[5]Myers, R. M., "Geometric Effects in Applied-Field MPD Thrusters," AIAA Paper 90-2669, July 1990.

[6]Sasoh, A., and Arakawa, Y., "Thrust Formula for an Applied-Field MPD Thruster Derived from Energy Conservation Equation," International Electric Propulsion Conf., IEPC-91-062, Oct. 1991.

[7]Peterkin, R. E., Jr., Giancola, A. J., and Sturtevant, J. E., "MACH2: A Reference Manual," 4th and 5th eds., Weapons Lab., Kirtland AFB, NM, Nov. 1986 and July 1992.

[8]Frese, M. H., "MACH2: A Two-Dimensional Magnetohydrodynamics Simulation Code for Complex Experimental Configurations," Rept. AMRC-R-874, NumerEx, Albuquerque, NM, Sep. 1986.

[9]Cranfill, C. W., "EOSPAC: A Subroutine Package for Accessing the Los Alamos Sesame EOS Data Library," Los Alamos, National Lab., LA-9728-M, Los Alamos, NM, Aug. 1983.

[10]Holian, K. S. (ed.), "T-4 Handbook of Material Properties Data Base, Vol Ic: EOS," Los Alamos National Lab., LA-10160-MS, Los Alamos, NM, Nov. 1984.

[11]Chapman, S., and Cowling, T. G., *The Mathematical Theory of Non-Uniform Gases*, 3rd ed., Cambridge Univ. Press, Cambridge, 1970, pp. 149–196.

[12]Mikellides, P. G., "A Theoretical Investigation of Magnetoplasmadynamic Thrusters," Ph.D. Dissertation, Dept. of Aeronautical and Astronautical Engineering, Ohio State Univ., Columbus, OH, Dec. 1994.

[13]Spitzer, L., *Physics of Fully Ionized Gases*, 2nd ed., Interscience, New York, 1962, pp. 81–86.

[14]Chodura, R., "A Hybrid Fluid-Particle Model of Ion-Heating in High Mach Number Shock Waves," *Nuclear Fusion Journal*, Vol. 15, No. 7, 1975, p. 55.

[15]Payne, S. S., "Two-Dimensional MHD Simulations of Magnetic Field Penetration in the Plasma Opening Switch," *IEEE Transactions on Plasma Science*, Vol. ps/15, No. 6, 1987, p. 725.

[16]Myers, R. M., Wehrle, D., Vernyi, M., Biaglow, J., and Reese, S., "A Preliminary Characterization of Applied-Field MPD Thruster Plumes," AIAA Paper 91-2339, June 1991.